Deep Learning Guided Autonomous Retinal Surgery using a Robotic Arm, Microscopy, and iOCT Imaging

Ji Woong Kim, Shuwen Wei, Peiyao Zhang, Peter Gehlbach, Jin U. Kang, Iulian Iordachita, Marin Kobilarov

***Abstract*—Recent technological advancements in retinal surgery has led to the modern operating room consisting of a surgical robot, microscope, and intraoperative optical coherence tomography (iOCT). The integration of these tools raises the fundamental question of how to effectively combine them to enable surgical autonomy. In this work, we address this question by developing a unified framework that enables real-time autonomous surgical workflows utilizing the aforementioned devices. To achieve this, we make the following contributions: (1) we develop a novel imaging system that integrates microscopy and iOCT in real-time, accomplished by dynamically tracking the surgical instrument via a small iOCT scanning region (e.g. B-scan), which was not previously possible; (2) implementing various convolutional neural networks (CNN) that automatically segment and detect task-relevant information for surgical autonomy; (3) enabling surgeons to intuitively select goal waypoints within both the microscope and iOCT views through simple mouse-click interactions; (4) integrating model predictive control (MPC) for real-time trajectory generation that respects kinematic constraints to ensure patient safety. We show the utility of our system by tackling subretinal injection (SI), a challenging procedure that involves inserting a microneedle below the retinal tissue for targeted drug delivery, a task surgeons find challenging due to requiring tens-of-micrometers of accuracy and precise depth perception. We validate our system by conducting 30 successful SI trials on pig eyes, achieving needle insertion accuracy of $26 \pm 12 \mu m$ to various subretinal goals and duration of 55 ± 10.8 seconds. Preliminary comparisons to a human operator performing SI in robot-assisted mode highlight the enhanced safety of our system.**

***Index Terms*—Vision-Based Navigation; Computer Vision for Medical Robotics; Medical Robots and Systems**

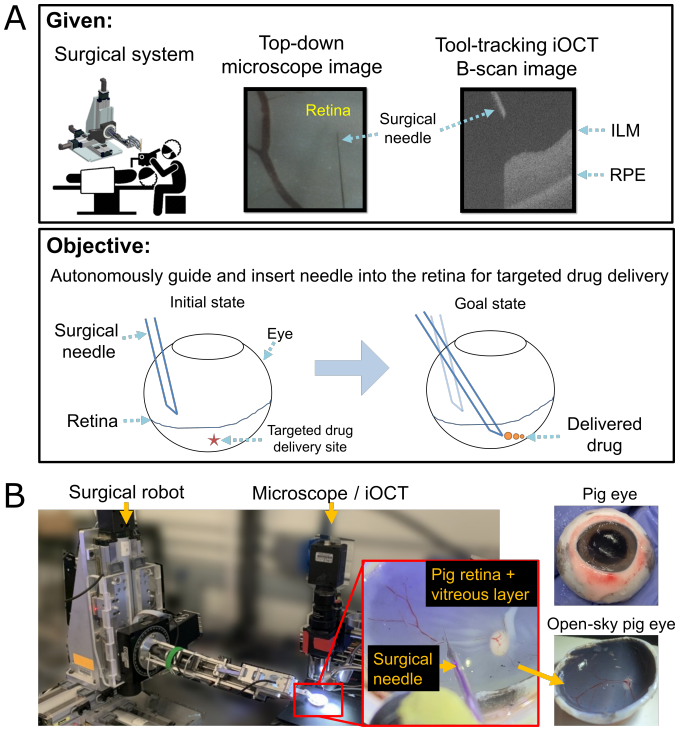

Fig. 1. (A) Problem statement (B) Experimental setup

I. Introduction

Subretinal injection (SI) is a surgical procedure that involves inserting a microneedle between the internal limiting membrane (ILM) and the retinal pigment epithelium (RPE) layer of the retina for targeted drug delivery (Fig. 1). Unlike the common intravitreal delivery method, which administer drugs above the retina and may not reach the desired subretinal space, SI offers greater effectiveness by delivering the drug in direct contact with the targeted subretinal tissue. However, SI presents several challenges. Surgeons must control their natural hand tremor ($\sim$180 μm in amplitude) [1], which are comparable to the thickness of the fragile retina ($\sim$200 μm) [2]. They must also deal with the lack of depth perception during needle insertion. Furthermore, during drug infusion, the needle-tip position must be maintained for extended periods, which risks damaging the retina due to the uncontrollable hand tremor. Consequently, SI pushes surgeons to their physiological limits.

To address the difficulties of SI, previous studies have introduced robotic assistance and intraoperative optical coherence tomography (iOCT) for depth guidance. iOCT is an imaging modality that provides cross-sectional (B-scan) or volumetric (C-scan) views of the surgical workspace, providing depth perception during needle navigation and insertion. Using such systems, prior works have demonstrated robot-assisted SI under teleoperated control by a surgeon [3]. More recently, more efforts have been made toward automating SI. For example, [4] and [5] developed workflows that allowed surgeons to select a goal waypoint in the iOCT view. The robot then navigated to

JW Kim, P. Zhang, I. Iordachita, and M. Kobilarov are with the Department of Mechanical Engineering, Johns Hopkins University, Baltimore, MD 21218 USA S. Wei and J. Kang are with the Department of Electrical and Computer Engineering, Johns Hopkins University, Baltimore, MD 21218 USA P. Gehlbach is with the Wilmer Eye Institute, Johns Hopkins University Hospital, Baltimore, MD 212187 USA

0000–0000/00$00.00 © 2021 IEEE

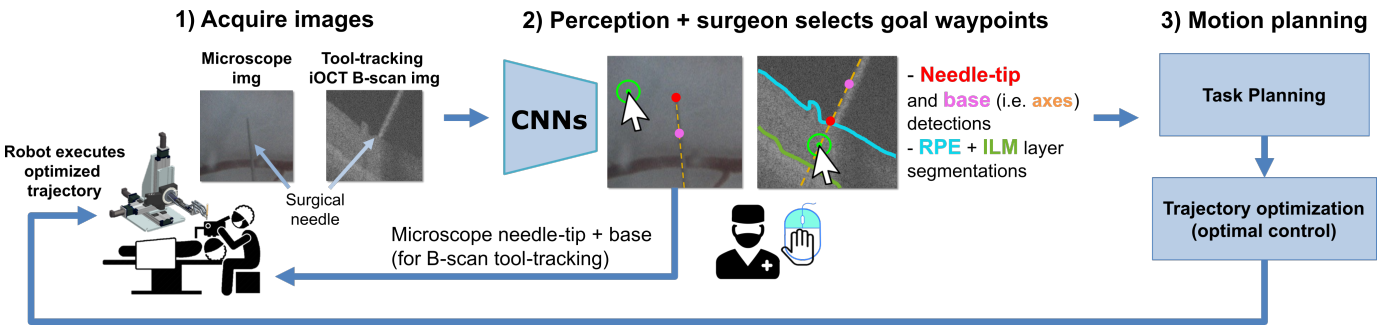

Fig. 2. High-level workflow: the microscope image and the iOCT B-scan images are acquired. Various CNNs provide task-relevant information for autonomy. The surgeon provides two waypoint goals in the microscope and B-scan images via mouse-clicks. Based on these information, the relevant task and motion is planned, and an optimized trajectory is sent to the robot for trajectory-tracking.

the selected waypoint below the retina to accomplish needle insertion, though relying on the limited pure transnational motion of the robot without enforcing safety-related kinematic constraints.

While there has been promising progress toward automation, significant challenges remain. This paper focuses on automating SI and thus we highlight the limitations of prior works in this area, specifically [4] and [5]. Firstly, these works lacked real-time capabilities due to reliance on slow volumetric C-scans. For instance, the state-of-the-art Leica iOCT system used in [5] required 7.69 seconds to scan a 2.5mm x 2.5mm (100 B-scans) square patch of the retinal region. Such scanning speed is inadequate considering the potential occurrence of involuntary patient motion and cyclic oscillations caused by patient breathing during that time period. Although relying on smaller C-scans or a single B-scan may be possible, the scanning region may become too limited, leading to the risk of losing sight of the surgical instrument or the target tissue due to patient motion. Furthermore, the small scanning regions could not be dynamically updated in real-time due to system constraints. Secondly, the mentioned prior works exclusively focused on utilizing iOCT views, neglecting the global and intuitive color view provided by the microscope. The microscope view should be utilized since surgeons can intuitively identify affected regions (e.g., bleeding areas), while this is not possible with iOCT as it only provides grayscale depth information. Lastly, these prior works did not account for the important remote-center-of-motion (RCM) constraint when designing their workflows and relied only on translational motion of the robot. It is crucial to enforce this surgical constraints to enable realistic and safe surgical workflows.

In this paper, we address these limitations by first developing a custom imaging system that integrates the microscope and iOCT in real-time by tracking the surgical instrument through a small iOCT scanning region. This is achieved by detecting the surgical instrument axis in the microscope image, and using this information to generate a B-scan aligned with the instrument axis. Even if the surgical tool moves, the B-scan automatically tracks the tool to provide real-time depth feedback. Ultimately, by combining microscopy and iOCT imaging, our system enables global and local awareness of the surgical workspace in real-time, offering both color and depth information. This conrtibution addresses the first two limitations mentioned above. We tackle the third limitation by employing this system to design a real-time workflow that incorporates the RCM constraint, ensuring patient safety. Our contributions include:

1) Designing a system and workflow for real-time autonomous SI that utilizes microscope and tool-axis-aligned B-scan images, with the B-scan dynamically tracking the tool axis to provide real-time depth feedback. RCM constraint is enforced to ensure patient safety.
2) Outlining a strategy for calibrating the microscope and iOCT to generate tool-axis-aligned B-scans.
3) Validating the system through 30 successful autonomous trials on 3 cadaveric pig eyes, achieving needle insertion accuracy of $26 \pm 12\mu m$ to various subretinal goals and duration of 55 ± 10.8 seconds. Preliminary comparisons to a human operator in robot-assisted mode demonstrate the improved safety of our system during needle-tissue interactions.

II. Related Works

iOCT has been used in several robot-assisted surgical applications, including corneal keratoplasty [6], vein cannulation [7], and subretinal injection [5] [4]. However, the common assumption across these works was that the iOCT (either used in C-scan and B-scan mode) was fixed on a predefined ROI. Given the speed limitations of acquiring C-scans or the limited view of B-scans, the proposed systems and workflows may not extend to dynamic settings where patient motion and instrument deformation are present, and thus dynamic update of the iOCT ROI is necessary. Our present work addresses this limitations by implementing a tool-tracking iOCT system, and additionally introducing the microscope view for global and intuitive view of the surgical workspace.

We also highlight a closely related work [8], which demonstrated real-time ROI update of the OCT B-scan and C-scan view by detecting a bounding box of the surgical tool from top-down spectrally encoded reflectometry (SER) images, in a similar fashion to our system. Our work, however, implements the calibration using microscope images and uses a different calibration approach. Also, their work primarily focused on developing an imaging system without robotic integration or experimental validation using animal tissues.

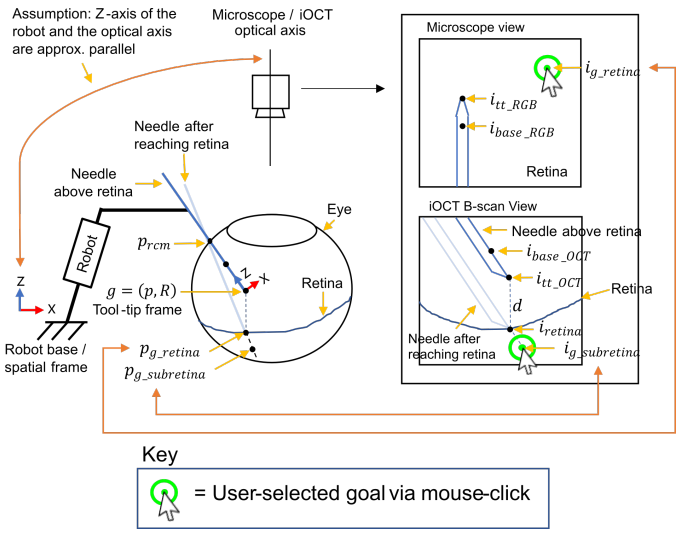

Fig. 3. Key variables used are shown. Double arrows are shown to indicate that the pixel goals i_{g_retina} and $i_{g\_subretina}$ correspond to p_{g_retina} and $p_{g\_subretina}$ respectively in euclidean space.

III. Problem Formulation

Consider a robotic manipulator with a surgical tool attached at its end-effector, as illustrated in Fig. 3. The key variables mentioned throughout this section are illustrated in Fig. 3. We define the robot states as $x = (g, V)$, where $g = (p, R) \in SE(3)$ and $V = (v, \omega) \in \mathbb{R}^6$. $p \in \mathbb{R}^3$ denotes the tool-tip position, $R \in SO(3)$ the orientation, and $v \in \mathbb{R}^3$ and $\omega \in \mathbb{R}^3$ the tool-tip-frame translational and angular velocity. Let the robot occupy a region $A(q) \subset \mathcal{W}$ in the workspace $\mathcal{W} \subset \mathbb{R}^3$, where q denotes the joint angles of the robot.

The tool-tip state x is fully-observable using high-precision motor encoders and precise knowledge of the robot forward kinematics. A given desired tool-tip velocity can be mapped to robot joint velocity to actuate the robot. Additionally, the system includes a monocular microscope camera generating top-down observations of the surgical environment $o_{RGB}(t) \in \mathcal{I}$ from space of images $\mathcal{I}$ at a given time t. A co-axially mounted OCT generates B-scan images $o_{OCT}(t) \in \mathcal{I}$. The B-scan plane dynamically tracks the tool such that the scanning plane is always aligned with the tool axis, thereby providing depth feedback between the needle and the underlying retina at all times.

Initially, the surgeon manually introduces the surgical tool into the eye through a sclera entry point, $p_{rcm} \in \mathbb{R}^3$, which is recorded at the time of entry. The sclera point should remain fixed after each entry to avoid unsafe forces exerted on the sclera tissue. Once the tool-tip is within the view of the microscope, its key points are detected in the microscope and B-scan views using two CNNs. Specifically, the detected tool-tip and its base are denoted as i_{tt_RGB}, $i_{base\_RGB} \in o_{RGB}(t)$ in the microscope image and i_{tt_OCT}, $i_{base\_OCT} \in o_{OCT}(t)$ in the B-scan image. These detected points also define the axis of the tools in the respective images (Fig. 2). Simultaneously, the retinal and RPE layers are segmented using another CNN, generating binary segmentation masks I_r and I_{RPE}. Using the detected tool-tip i_{tt_OCT} and the segmented retinal layer I_r, the projection of the tool-tip to the retinal layer directly below (i.e. along the same image column index) is computed and denoted i_{retina} in the B-scan view.

Given this setup, the surgeon then selects a 2D pixel goal $i_{g\_retina} \in o_{RGB}(t)$ via a mouse-click in the top-down microscope image. This goal denotes the desired waypoint through which the needle is introduced into the retina from the microscope view. It also corresponds to a 3D euclidean point $p_{g\_retina} \in \mathcal{W}$ on the surface of the retina w.r.t the robot's spatial frame. We seek to reach p_{g_retina}, however, its exact location is unknown. Instead of estimating p_{g_retina} directly, we propose to reach it approximately by employing a specific visual-servoing strategy (Section IV). After p_{g_retina} is reached using this strategy, the surgeon specifies another goal waypoint $i_{g\_subretina} \in o_{OCT}(t)$ along the axis of the needle and below the retina in the B-scan view via a mouse-click. Note that at this point, the needle is placed on the retinal surface, as illustrated in Fig. 3 (labelled as "Needle after reaching retina"). The goal $i_{g\_subretina}$ corresponds to a 3D euclidean point $p_{g\_subretina} \in \mathcal{W}$ defined w.r.t the robot spatial frame. This subretinal goal is the target drug-delivery site. Since the iOCT B-scan is always aligned with the needle-axis, $p_{g\_subretina}$ can be reached by simply inserting the needle along its axis.

In summary, the objective is to navigate the needle-tip to two sequential goals: p_{g_retina} and then $p_{g\_subretina}$, given the user-clicked goals i_{g_retina} and $i_{g\_subretina}$ respectively. We thus consider the following two problems:

1) *Navigating the needle above the retinal surface*: navigate the needle-tip to the desired needle insertion point on the retinal surface p_{g_retina} given the clicked goal i_{g_retina}.
2) *Needle insertion*: insert the needle along its axis to reach the goal insertion waypoint $p_{g\_subretina}$ given the clicked goal $i_{g\_subretina}$.

The objective is to autonomously perform the above tasks while relying on a monocular top-down images, tool-axis aligned B-scan images, and various perception modules automatically providing the state of the surgical environment. Additionally, kinematic constraints concerned with the safety of the surgery must be satisfied while ensuring smooth robot motion.

IV. Technical Approach

A. Navigation above the retina

The first step of the navigation procedure is positioning the needle-tip at the first desired waypoint p_{g_retina} given the user-selected goal i_{g_retina}. Recall that i_{g_retina} is only a 2D pixel goal, therefore the corresponding 3D location p_{g_retina} is unknown. The usual approach in this setting is to estimate p_{g_retina} using sensors, which can be challenging considering the presence of unknown distortions caused by the vitreous, the cornea, and the lens (in our open-sky eye scenario, only the vitreous). Instead, we propose a straight-forward navigation procedure which p_{g_retina} can be approximately reached without directly estimating its 3D position. At a high level, this procedure first consists of aligning the needle-tip with the clicked goal i_{g_retina} via 2D planar motion in the top-down

microscope view. Then, the needle is simply lowered towards the retina while relying on the B-scan for depth feedback. The procedure is as follows:

Step 1: Align the needle-tip with the clicked goal i_{g_retina} via 2D visual-servoing i.e. via actutation *only* along the robot's spatial XY plane (the robot's spatial XY frame is shown in Fig. 3). This step effectively aligns the needle-tip with the clicked goal pixel i_{g_retina} in the top-down microscope view.

Step 2: Lower the needle towards the retinal surface via incremental motion along the robot's spatial Z-axis. This step moves the needle-tip closer to the retinal surface in the B-scan view, while mostly keeping the needle-tip aligned with the clicked goal in the microscope view.

Step 3: Repeat the above two steps until i_{retina} (Fig. 3) is reached in the B-scan view.

The underlying assumption here is that the optical axis of the microscope and the robot's spatial Z-axis are approximately parallel, as illustrated in Fig. 3. Therefore, during 2D planar motion (step 1), the observed motion of the needle-tip is a corresponding planar motion in the microscope image. During the needle lowering step (step 2), the observed motion is a corresponding needle-lowering motion in the B-scan view. However, during step 2, the tool-tip may deviate from the clicked goal in the microscope view, since the optical axis and the robot's spatial Z-axis are only approximately parallel. Therefore, steps 1 and 2 must be repeated (step 3) whenever a pixel error above a small threshold is observed to realign the needle-tip with the clicked goal. In our experiments, we chose this threshold to be 1 pixel. Ultimately, this iterative procedure enables accurate placement of the needle-tip anywhere on the retinal surface. Note that to achieve step 1, calibration between the robot and the microscope is necessary, which is described in Section IV-D.

B. Needle insertion

Once the needle-tip is approximately placed on the desired location on the retinal surface p_{g_retina} (Section IV-A), the surgeon specifies another goal waypoint $i_{g\_subretina}$ in the B-scan view via a mouse click. Note that at this point in time, the needle is placed on the retinal surface at the desired clicked location i_{g_retina}. The desired insertion distance is obtained as follows:

$$d_{insertion} = \|i_{g\_subretina} - i_{tt\_OCT}\|^2. \tag{1}$$

n The pixel distance is converted to microns using a conversion factor (Table I). The needle is then inserted along its axis to reach $p_{g\_subretina}$.

C. Microscope-OCT Calibration

The microscope-OCT setup combines a 100 kHz swept source OCT system [9] with a microscope for simultaneous OCT and microsopic imaging. A charged-coupled device (CCD) is added to the OCT system to capture microscopic images [10]. Both the OCT and the CCD share the same objective lens, ensuring precise alignment and consistent working distance. A short-pass dichroic mirror with a 650 nm cutting-off wavelength splits the light into reflection and transmission. It reflects near infrared light back to the OCT system while transmitting visible light to the CCD for microscopic imaging. The transmitted visible light is focused onto the CCD by an imaging lens, and a short-pass filter is employed to reduce near infrared noise. Two galvo mirrors are utilized to tilt the collimated beam from the fiber collimator, and thus control the OCT scanning position. This integrated microscope-OCT setup facilitates a comprehensive OCT and microscopic visualization.

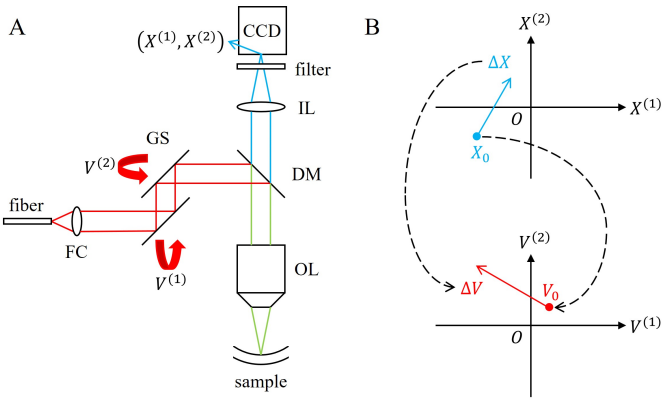

Fig. 4. (A) Microscope-OCT system setup. FC, fiber collimator; GS, galvo scanners; DM, dichroic mirror; IL, imaging lens; OL, objective lens. (B) The mapping between the laser scanning position and the applied voltage.

The laser scanning position in a microscopic image is determined by the rotation angles of two orthogonal galvo mirrors, which are controlled through voltages. We assume a linear relationship between the laser scanning position and the applied voltages, given by the equation:

$$X = RV + T, \tag{2}$$

where $X = \begin{bmatrix} X^{(1)} & X^{(2)} \end{bmatrix}^\intercal \in \mathbb{R}^2$ represents the laser scanning position in the microscopic image, $V = \begin{bmatrix} V^{(1)} & V^{(2)} \end{bmatrix}^\intercal \in \mathbb{R}^2$ corresponds to the voltages applied to the two galvo mirrors, $R \in \mathbb{R}^{2\times 2}$ and $T \in \mathbb{R}^2$ are linear parameters that convert the applied voltages to the corresponding laser scanning position in the microscopic image. The mapping between the laser scanning position and the applied voltage is shown in Fig. 4(b).

The linear parameters R and T need to be calibrated. We use a laser viewing card to visualize and locate the laser scanning position in the microscopic image. We record a set of laser scanning positions $\{X_i | i \in \{1, \ldots, N\}\}$ when applying voltages according to a predefined voltage set $\{V_i | i \in \{1, \ldots, N\}\}$. The linear parameters R and T are calibrated by minimizing the least square error:

$$\hat{R}, \hat{T} = \underset{R,T}{\operatorname{argmin}} \sum_{i=1}^{N} ||RV_i + T - X_i||_2^2, \tag{3}$$

where $||\cdot||_2$ refers to Euclidean norm. It can be derived that:

$$\hat{R}^\intercal = (\mathbb{V}\mathbb{V}^\intercal)^{-1}\mathbb{V}\mathbb{X}^\intercal, \tag{4}$$

$$\hat{T} = \bar{X} - \hat{R}\bar{V}, \tag{5}$$

where $\mathbb{V} \in \mathbb{R}^{2\times N}$ and $\mathbb{V} \in \mathbb{R}^{2\times N}$ are matrices that are expressed as:

$$\mathbb{V} = \begin{bmatrix} V_1 - \bar{V} & V_2 - \bar{V} & \cdots & V_N - \bar{V} \end{bmatrix}, \tag{6}$$

$$\mathbb{X} = \begin{bmatrix} X_1 - \bar{X} & X_2 - \bar{X} & \cdots & X_N - \bar{X} \end{bmatrix}, \tag{7}$$

and $\bar{V} = \frac{1}{N}\sum_{i=1}^{N} V_i$, $\bar{X} = \frac{1}{N}\sum_{i=1}^{N} X_i$.

To generate OCT B-scan that is aligned with the needle axis in the microscopic image, we need the needle tip position, needle orientation and a predefined scanning length in the microscopic image frame. The central voltage is determined by:

$$V_0 = \hat{R}^{-1}(X_0 - \hat{T}), \tag{8}$$

where $X_0 \in \mathbb{R}^2$ is the needle tip position in the microscopic image. The voltages are determined on the tangent space at V_0 through the equation:

$$\Delta V = \hat{R}^{-1}\Delta X, \tag{9}$$

where ΔV is the tangent vector at V_0 describing the voltage amplitude and the voltage angle, and ΔX is the tangent vector at X_0 describing the needle orientation and the predefined scanning length. Therefore, to generate a scanning cross section along the needle axis and centered at the needle tip that is described by:

$$X(t) = X_0 + t\Delta X, \tag{10}$$

where $t \in (-1, 1)$ is a normalized time parameter, we should control the voltage according to:

$$V(t) = V_0 + t\Delta V, \tag{11}$$

where V_0 and ΔV are determined by Eq. 8 and Eq. 9, respectively.

D. Real-Time Hand-Eye Calibration and Visual Servoing

In order to navigate the needle-tip to the clicked goal i_{g_retina} (i.e. during step 1 in Section IV-A), the calibration parameters between the robot and the microscope must be ascertained. To avoid complex calibration procedure such as in [4], we choose a visual servoing strategy which relies on real-time iterative updates to the calibration matrix based on the observed robot motions in real-time [11]. This effectively enables real-time adaptation to the changing intrinsic and extrinsic properties of the camera, enabling the surgeon to change the microscope position, magnification, or add distortive optics (e.g. BIOME or contact-lenses) during the procedure, without needing to perform a calibration procedure repeatedly when any of these parameters change.

Since the robot's spatial Z-axis and the camera's optical axis are approximately parallel (Section IV-A), the calibration is only performed between the robot's spatial XY plane and the image plane. To simplify the notation, we introduce a variable $\bar{p} = Sp \in \mathbb{R}^2$, which simply denotes the XY components of the surgical tool-tip position, where the selector matrix $S \in \mathbb{R}^{2\times 3}$ picks out the first two elements of the vector it operates on. S is defined as:

$$S = \begin{bmatrix} 1 & 0 & 0 \\ 0 & 1 & 0 \end{bmatrix}. \tag{12}$$

Consider an unknown function $K : \mathbb{R}^2 \to \mathbb{R}^2$ which converts the tool-tip XY position to its corresponding image coordinates. K implicitly contains the intrinsic and extrinsic parameters of the camera. In other words,

$$i_{tt\_RGB} = K(\bar{p}). \tag{13}$$

We may approximate the unknown K using the first-order Taylor series approximation:

$$K(\bar{p}^{k+1}) \approx K(\bar{p}^k) + J_{calib}(\bar{p}^k)(\bar{p}^{k+1} - \bar{p}^k) \tag{14}$$

$$\Delta i^k_{tt\_RGB} \approx J_{calib}(\bar{p}^k)(\Delta\bar{p}^k) \tag{15}$$

where J_{calib} is a Jacobian matrix that relates the change in tool-tip XY position $\Delta\bar{p}^k$ to the corresponding change in image coordinates $\Delta i^k_{tt\_RGB}$. k denotes the iteration step, since the Jacobian is a local approximation at a particular time step. Specifically, the Jacobian is recalculated whenever a significant change $\Delta i^k_{tt\_RGB}$ and $\Delta\bar{p}^k$ is observed (i.e. when robot motion observed).

Borrowing from [11], we use an online update rule to estimate the Jacobian in real-time based on the observed robot motions. The method utilizes Broyden's update formula to estimate the Jacobian, given as:

$$J^{k+1}_{calib} = J^k_{calib} + \beta\frac{\Delta i^k_{tt\_RGB} - J^k_{calib}\Delta\bar{p}^k}{(\Delta\bar{p}^k)^T(\Delta\bar{p}^k)}(\Delta\bar{p}^k)^T, \tag{16}$$

where $0 \leq \beta \leq 1$ is the step size for updating the Jacobian [12]. We chose $\beta = 0.5$. This is an iterative approach where the Jacobian is initialized as an arbitrary non-singular matrix (e.g. an identity matrix) and after several updates it converges to the true Jacobian. To use the Jacobian to guide the needle to i_{g_retina}, we reformulate Eq. 15 as

$$\Delta\bar{p}_{desired} = J_{calib}(\bar{p}^k)^{-1}\Delta i_{desired}, \tag{17}$$

where $\Delta i_{desired} = i_{g\_retina} - i_{tt\_RGB}$ is the desired motion vector in image coordinates, and $\bar{p}_{desired}$ is the desired change in tool-tip position to align the needle-tip with the clicked goal.

Using $\Delta\bar{p}_{desired}$, the desired waypoint to reach can be given as:

$$p_{desired} = p + \begin{bmatrix} \Delta\bar{p}_{desired} \\ 0 \end{bmatrix}. \tag{18}$$

where the motion along robot's spatial Z-axis is zero. To be clear, $p_{desired} \neq p_{g\_retina}$. $p_{desired}$ can be considered as an intermediate waypoint that is constantly updated (e.g. every time the Jacobian is updated), such that the tool-tip will be eventually aligned with i_{g_retina} in the microscope view.

E. Optimal Control Formulation

Once a desired goal waypoint $p_{desired}$ is determined (Section IV-D) it is used by an optimal control framework to generate an optimal trajectory to the goal. Formally, we seek

to generate an tool-tip trajectory $x([t_0, t_f])$ over some time-interval $[t_0, t_f]$:

$$\underset{x(\cdot),u(\cdot)}{\operatorname{argmin}} \int_{t_0}^{t_f} C(x(t), u(t))dt, \quad \text{:minimize cost} \tag{19}$$

$$\dot{x}(t) = f(x(t), u(t)), \quad \text{:system dynamics} \tag{20}$$

$$(I - r_z(t)r_z(t)^T)(p_{rcm} - p(t)) = 0, \quad \text{:sclera constraint} \tag{21}$$

where $C(x, u)$ is a given cost function e.g. ensuring smooth motion, and $r_z = Re_z$ and $e_z = (0, 0, 1)$ is the third basis vector (i.e. the surgical tool's longitudinal axis in the tool-tip frame). The system dynamics is modeled as a fully-actuated rigid body with three translational and rotational forces acting on itself. To solve this optimal control problem reliably in real-time we re-formulate it to include the constraint (21) as a least-square penalty, according to:

$$\begin{aligned} C = &\frac{1}{2}\|p_f - p(t_f)\|^2_{P_f} + \int_{t_0}^{t_f} \frac{1}{2}\|u(t)\|^2_R \\ &+ w_s \cdot \|(I - r_z(t)r_z(t)^T)(p_{rcm} - p(t))\|^2 \mathrm{d}t, \end{aligned} \tag{22}$$

where $p_f = p_{desired}$. Specifically, $p_{desired}$ is determined following the formulation given in Section IV-D. In general, the overall cost aims to minimize the error in reaching the goal (encoded using $P_f \geq 0$ gain matrices), control effort (using $R > 0$ gain matrix) and penalize deviation from the sclera point (using weight w_s). The optimal control problem is solved numerically using differential dynamic programming (DDP) based on a discrete-time quantization of the robot motion using some fixed time-step dt, over which the discrete controls are assumed to be constant [13]. The resulting optimization generates a discrete sequence of states and controls, $x_{0:N_{traj}} \triangleq \{x_0, \cdots, x_{N_{traj}}\}$ and $u_{0:N_{traj}-1} \triangleq \{u_0, \cdots, u_{N_{traj}-1}\}$, where $N_{traj} = 64$. The optimized trajectory is then used in a low-level controller to track the trajectory.

F. Network Training

Two CNNs are implemented for the tool-tip and its base predictions (Fig. 5A). One network is used for the microscope images and another network for the B-scan images. Both networks are identical and adopt a U-Net-like [14] architecture, using Resnet-18 [15] as a backbone. After the image is encoded into feature vectors, two decoders are used to predict the tool-tip and its base respectively. The output sizes are identical to the input sizes ($480 \times 640 \times 3$ and 1024×512 for the microscope and B-scan images respectively). In order to enforce consistency, the distance between the tool-tip and its base are set to be 50 and 100 pixels in the microscope and B-scan images respectively.

We implement a third CNN to segment the retinal and the RPE layer of the B-scan, as shown in Fig. 5B. This segmentation network is identical as before, but the decoder now outputs three channels, predicting the background, retinal layer, and the RPE layer respectively.

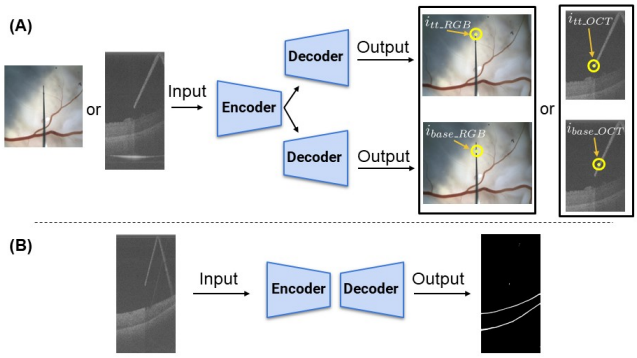

Fig. 5. Network architectures: (A) Two networks are trained to detect the needle tip and its base (thus defining its axis), one for microscope and another for iOCT images. (B) A third network is trained to the ILM and RPE layer segmentations

To train the networks, cross-entropy loss was used for the tool-tip and its base predictions and the retinal layers segmentation. For the tool-tip and its base predictions, an additional MSE loss was used to enforce consistent distance spacing between the predicted points (i.e. 50 or 100 pixels). Also, to balance the errors among the three labels during segmentation training, we set the weights for the background, ILM, and RPE layer to be 0.001, 0.4995, and 0.4995 respectively. 2000 microscope images and 1050 B-scan images were used for training. Adam optimizer with a learning rate of 0.0003 was used.

V. Experiments

As shown in Fig. 1B, the experimental setup consists of the Steady Hand Eye Robot (SHER) [16], a silver-coated glass pipette attached at the robot handle ($30\mu m$ tip diameter), a microscope-integrated OCT, and an open-sky pig eye filled with vitreous.

We validated our system through 30 autonomous subretinal injection trials on 3 open-sky pig eyes (Fig. 1B). For each eye, 10 trials were performed. The experimental procedure follows the description provided in Section III. We evaluate our system based on the following metrics:

TABLE I
Conversion factors for converting pixel distance to microns

Image Type	Conversion factor (μm / pixel)
Microscope image	13.6
B-scan (along img height)	2.6
B-scan (along img width)	5.3
B-scan (between B-scan slices)	13.6

1) **Navigation error on the retinal surface goal** (Fig. 6A): this metric measures how closely the needle-tip is placed on the retinal surface goal p_{g_retina} after performing the navigation procedure described in Section IV-A. Recall that we did not estimate of p_{g_retina} directly. Therefore, we approximate the error by combining the 2D navigation error between the clicked goal (i_{g_retina}) and the needle-tip (i_{tt_RGB}) in the microscope view and the depth error between the needle-tip

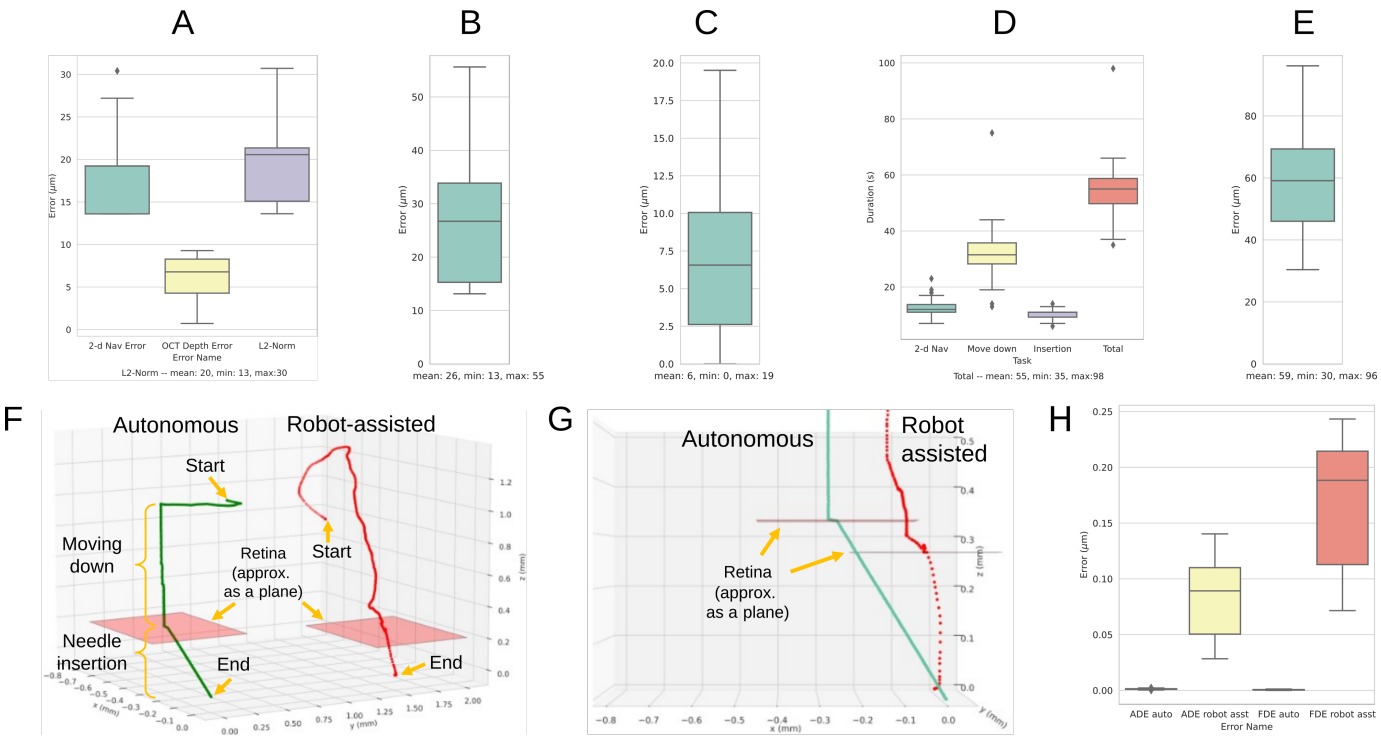

Fig. 6. Experimental metrics are shown: (A) navigation error on the retinal surface goal (B) needle-insertion error at the drug delivery site (C) RCM error (D) total duration of the surgery by task (E) 2D navigation error to the clicked goal from the microscope view during robot-assisted mode (F) qualitative comparison between autonomous and robot-assisted modes (G) same comparison from a close-up side view during needle insertion (H) comparing the deviation of the needle-tip from the insertion axis during needle insertion; ADE (average displacement error), FDE (final displacement error).

(i_{tt_OCT}) and the retinal goal (i_{g_retina}) in the B-scan view to obtain the navigation error in 3D.

Specifically, we compute the 2D navigation error in the microscope view using the following formula (2D Nav Error in Fig. 6A): $\|i_{g\_retina} - i^*_{tt\_RGB}\|_2$, where $i^*_{tt\_RGB}$ is the ground-truth needle-tip pixel obtained via manual annotation. We compute the depth error using the B-scan view via the following formula (OCT Depth Error in Fig. 6A): $\|\bar{S}^T i_{retina} - \bar{S}^T i^*_{tt\_OCT}\|_2$, where $i^*_{tt\_OCT}$ is the ground-truth needle-tip pixel in the B-scan view obtained via manual annotation, and $\bar{S}$ is a selector vector that picks out the second element of the vector it operates on (i.e. the pixel index along the B-scan image height). Specifically, $\bar{S} = [0\ 1] \in \mathbb{R}^2$. Finally, these two errors are combined using the L2-norm metric (L2-Norm in Fig. 6A). The computed pixel errors are converted into microns using the relevant conversion factors listed in Table I.

2) **Needle insertion error** (Fig. 6B): this metric measures how closely the needle-tip reaches the desired insertion goal below the retina $p_{g\_subretina}$ based on the acquired volume scans after needle insertion. The error is calculated using the following L2-norm metric: $\|[i^T_{g\_subretina}\ gt\_slice] - [i^{*T}_{tt\_OCT}\ actual\_slice]\|_2$, gt_slice is the ground-truth B-scan slice index which the needle is expected to land and $actual\_slice$ is the B-scan slice index which the needle actually lands after needle insertion. The computed voxel errors are converted to microns using the relevant conversion factors in Table I. Note that a volumetric scan was performed after needle insertion (i.e. multiple B-scans or "slice" of images were collected) to compute this error.

3) **RCM error** (Fig. 6C): this metric measures how closely the needle-axis is aligned with the RCM point throughout the entire procedure, computed using Eq. 21.

4) **Task duration** (Fig. 6D): this metric measures the duration taken for each task and their total sum.

VI. Results and Discussion

We provide more details on the results and the metrics provided in Section V. During the 30 autonomous SI trials, the needle-tip could reach the desired retinal surface goal p_{g_retina} with $20 \pm 6\mu m$ accuracy w.r.t the L2-norm metric as shown in Fig. 6A. As shown in Fig. 6B, the error in reaching the subretinal goal $p_{g\_subretina}$ was $26 \pm 12\mu m$. Note that reaching the desired depth is the most critical requirement in terms of safety while reaching $p_{g\_subretina}$, to avoid potential damage to the retina, and the error along the depth dimension was $7 \pm 11\mu m$. In comparison, such level of accuracy may be difficult to achieve for human surgeons, considering that the mean hand-tremor amplitude during retinal surgery is approximately $180\mu m$ [1]. While the results are promising, we expected lower error in reaching the subretinal goal $p_{g\_subretina}$. The error appears to be caused by the needle not being perfectly mounted on the end-effector, due to using an imprecise bracket for mounting. This misalignment can cause the needle to move in a direction not aligned with its tip axis, therefore leading to such targeting errors during insertion. In future work, this

error may be reduced by changing to a more precise setup for mounting the needle.

Throughout the entire procedure, the RCM error was kept low at $6 \pm 4\mu m$ as shown in Fig. 6C. Note that the RCM errors are calculated based on robot kinematics using Eq. 21, therefore, the true observed RCM error may be slightly larger. Finally, the total duration of the surgery was 55 ± 10.8 seconds as shown in Fig. 6D. Note that the measured time captures the navigation and insertion procedure, excluding the drug-infusion step which could take up to additional minutes in practice.

We also show a preliminary comparison to a human performing SI in robot-assisted mode. In robot-assisted mode, the human operator controlled the robot by placing the hand at the end-effector and modulating the gain of the motion using a foot pedal, and 10 trials were performed. The robot-assisted mode follows the control scheme originally developed in [16]. Qualitatively, as shown in Fig. 6F, the autonomous trajectory is more stable and efficient. Quantitatively, the robot-assisted trajectory is less accurate in being able to reach the top-down clicked goal. Specifically, the navigation error for robot-assisted mode is $59 \pm 19\mu m$ (Fig. 6E), while for autonomous mode it is $19 \pm 6\mu m$ (2D Nav Error in Fig. 6A). A closer side view comparison in Fig. 6G shows that, for the autonomous mode, the needle insertion trajectory is nearly perfect along the needle's axis. However, this is difficult to achieve in robot-assisted mode, since this constraint is difficult for humans to enforce by hand. We quantitatively show the deviation of the needle-tip trajectory from the originally intended insertion axis in Fig. 6H. Specifically, we consider a commonly-used average displacement (ADE) and final displacement error (FDE) metric for comparing trajectories. ADE computes the averaged L2-norm distance between the originally-intended insertion axis trajectory and the executed trajectory, and FDE computes the L2-norm error between them only at the last waypoint of each trajectory. We can see that both ADE and FDE errors are near zero in autonomous mode. However, in robot-assisted mode, the errors are in the order of hundreds of micrometers. In summary, the autonomous mode is able to execute a more smooth and stable motion, while keeping the needle trajectory constrained along its axis, thereby inflicting minimal damage on the retina.

We also note that while all 30 autonomous trials were successful, 2 trials required human intervention. Intervention was necessary during the initial 2D navigation step due to perception error, when the CNN randomly failed to detect the needle-tip position. When this occurred, the operator simply intervened and initialized the needle at a different location above the retina and the trial was resumed. This error did not lead to any damage on the retina, since the errors occurred during the 2D navigation step above the retinal surface. To avoid this, more efforts should be invested in improving the robustness of the CNN's predictions. However, this work requires intensive labor for collecting a large dataset and manually labelling them, which is out-of-scope in this paper. We thus leave this point of improvement for future work.

VII. Conclusion

In this work, we demonstrated a real-time, autonomous system and workflow for subretinal injection. This was enabled by the global view provided by microscope images and a dynamically-aligned B-scans that tracked the needle axis for real-time depth feedback. Future work will consider extending this work to closed pig eye settings, and extending this framework to tackle more challenging tasks such as grasping or peeling the retinal membrane.

References

[1] S. Singh and C. Riviere, "Physiological tremor amplitude during retinal microsurgery," in *Proceedings of the IEEE 28th Annual Northeast Bioengineering Conference (IEEE Cat. No.02CH37342)*, 2002, pp. 171–172.

[2] A. Chan, J. S. Duker, T. H. Ko, J. G. Fujimoto, and J. S. Schuman, "Normal macular thickness measurements in healthy eyes using stratus optical coherence tomography," *Arch. Ophthalmol.*, vol. 124, no. 2, pp. 193–198, Feb. 2006.

[3] J. Cehajic-Kapetanovic, K. Xue, T. L. Edwards, T. C. Meenink, M. J. Beelen, G. J. Naus, M. D. de Smet, and R. E. MacLaren, "First-in-human robot-assisted subretinal drug delivery under local anesthesia," *Am. J. Ophthalmol.*, vol. 237, pp. 104–113, May 2022.

[4] K. Mach, S. Wei, J. W. Kim, A. Martin-Gomez, P. Zhang, J. U. Kang, M. A. Nasseri, P. Gehlbach, N. Navab, and I. Iordachita, "Oct-guided robotic subretinal needle injections: A deep learning-based registration approach," in *2022 IEEE International Conference on Bioinformatics and Biomedicine (BIBM)*. IEEE, 2022, pp. 781–786.

[5] S. Dehghani, M. Sommersperger, P. Zhang, A. Martin-Gomez, B. Busam, P. Gehlbach, N. Navab, M. A. Nasseri, and I. Iordachita, "Robotic navigation autonomy for subretinal injection via intelligent real-time virtual ioct volume slicing," 2023.

[6] B. Keller, M. Draelos, K. Zhou, R. Qian, A. N. Kuo, G. Konidaris, K. Hauser, and J. A. Izatt, "Optical coherence tomography-guided robotic ophthalmic microsurgery via reinforcement learning from demonstration," *IEEE Transactions on Robotics*, 2020.

[7] M. J. Gerber, J.-P. Hubschman, and T.-C. Tsao, "Automated retinal vein cannulation on silicone phantoms using optical-coherence-tomography-guided robotic manipulations," *IEEE/ASME Transactions on Mechatronics*, vol. 26, no. 5, pp. 2758–2769, 2021.

[8] E. M. Tang, M. T. El-Haddad, S. N. Patel, and Y. K. Tao, "Automated instrument-tracking for 4d video-rate imaging of ophthalmic surgical maneuvers," *Biomed. Opt. Express*, vol. 13, no. 3, pp. 1471–1484, Mar 2022. [Online]. Available: https://opg.optica.org/boe/abstract.cfm?URI=boe-13-3-1471

[9] S. Wei, S. Guo, and J. U. Kang, "Analysis and evaluation of bc-mode oct image visualization for microsurgery guidance," *Biomedical optics express*, vol. 10, no. 10, pp. 5268–5290, 2019.

[10] S. Wei, J. W. Kim, A. Martin-Gomez, P. Zhang, I. Iordachita, and J. U. Kang, "Region targeted robotic needle guidance using a camera-integrated optical coherence tomography," in *Optical Coherence Tomography*. Optica Publishing Group, 2022, pp. CM2E–6.

[11] M. J. agersand and R. C. Nelson, "Adaptive differential visual feedback for uncalibrated hand-eye coordination and motor control," 1994.

[12] C. G. Broyden, "A class of methods for solving nonlinear simultaneous equations," *Mathematics of Computation*, vol. 19, pp. 577–593, 1965.

[13] M. B. Kobilarov and J. E. Marsden, "Discrete geometric optimal control on lie groups," *IEEE Transactions on Robotics*, vol. 27, no. 4, pp. 641–655, 2011.

[14] O. Ronneberger, P. Fischer, and T. Brox, "U-net: Convolutional networks for biomedical image segmentation," in *Medical Image Computing and Computer-Assisted Intervention*. Springer, 2015, pp. 234–241.

[15] K. He, X. Zhang, S. Ren, and J. Sun, "Deep residual learning for image recognition," in *Proceedings of the IEEE conference on computer vision and pattern recognition*, 2016, pp. 770–778.

[16] A. Üneri, M. A. Balicki, J. Handa, P. Gehlbach, R. H. Taylor, and I. Iordachita, "New steady-hand eye robot with micro-force sensing for vitreoretinal surgery," in *Biomedical Robotics and Biomechatronics (BioRob), 2010 3rd IEEE RAS and EMBS International Conference on*. IEEE, 2010, pp. 814–819.